

**Emission-Computed Tomography and Its Application to
Imaging of Acute Myocardial Infarction in Intact Dogs
Using Tc-99m Pyrophosphate**

Manbir Singh, Michael J. Berggren, David E. Gustafson, Mrinal K. Dewanjee, Robert C. Bahn, and Erik L. Ritman

*University of Southern California, Marina del Rey, California, and Mayo Clinic and Mayo Foundation,
Rochester, Minnesota*

The techniques of emission-computed tomography have been used to obtain in vivo quantitative estimates of the three-dimensional distribution of gamma-emitting radionuclides in dog hearts. Conjugate views, obtained for 60 equiangular projections around 360° by rotating the object in front of a gamma camera, were used to reconstruct multiple-level emission transaxial images for various test objects, and for dogs with surgically induced acute myocardial infarcts. Corrections for attenuation were performed in the backprojection step of the convolution algorithm used for reconstruction. Quantitative estimates of the spatial extent and concentration of activity were obtained to within 10–15% rms error. Correlations were obtained between the radionuclide and histopathologic estimates of the extent and location of infarction.

J Nucl Med 20: 50–56, 1979

The techniques of computerized transaxial imaging can be used to obtain an in vivo quantitative estimate of the distribution of radionuclides in three dimensions, thereby overcoming superposition problems inherent in conventional two-dimensional projection images. Kuhl and Edwards (1) were the first to demonstrate transaxial reconstruction of gamma-emitting radionuclides in 1963 by using simple backprojection of profile data collected at multiple angles with a rectilinear scanner. Several reconstruction algorithms, either iterative or based

on convolution with a filter function, have since been developed and applied to obtain quantitative or semi-quantitative estimates of single-gamma or positron-emitting radionuclides (2,3). Either gamma cameras (4–6), or arrays of NaI(Tl) crystals with lead collimation (7), or multicrystal positron cameras based on electronic collimation (8–11) are used in these studies. The quantitative aspects of results obtained with single-gamma emitters have been questioned by several investigators because of a) variation of resolution (line spread function) and sensitivity as a function of distance from the collimator, and b) lack of an accurate method to correct for attenuation of the radiation by the tissues (12, 13). We have developed a procedure for minimizing the variation of sensitivity and resolution with

Received May 4, 1978; revision accepted Aug. 11, 1978.

For reprints contact: Manbir Singh, University of Southern California, Medical Imaging Science Group, 4676 Admiralty Way, Suite 932, Marina del Rey, CA 90291.

depth and for making corrections for attenuation in a reconstruction scheme using a filtered backprojection technique. Multiple-level transaxial images of single-gamma emitters were obtained with this technique from various test objects and from dogs in which acute myocardial infarcts (AMI) were surgically induced. This method has produced quantitative transaxial emission images (rms uncertainty of about 10%) for single-gamma emitters. This paper briefly describes the reconstruction procedure and results obtained with the test objects and seven dogs (six with AMI, one control) using an i.v. injection of Tc-99m-pyrophosphate (PPI). A large-field-of-view gamma camera with a low-energy, all-purpose, parallel-hole collimator was used for all of these studies, and for the animal studies a prototype cylindrical x-ray tomographic scanner (14) was used to determine attenuation coefficients for the attenuation-correction method.

Reconstruction procedure. Emission profile data were collected at multiple angles of view by rotating the object in front of the gamma camera. The images obtained therefrom were digitized on a 64 by 64 grid with 7-mm spacing between pixels, thus affording up to 64 adjacent levels for transaxial reconstruction. The following procedure was adopted to minimize the variation of line spread function and sensitivity with depth, and to correct for attenuation of photons by the tissues.

Variation of line spread function and sensitivity with depth. The line spread functions for the present camera and collimator assembly were measured as a function of distance from the collimator, both in air and water and are presented in Fig. 1. Following the lead of Kay and Keys (15), we have used the

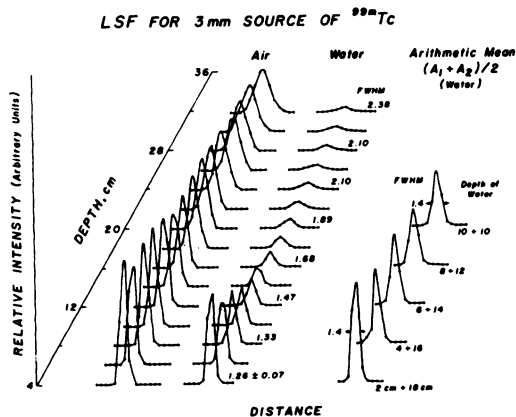


FIG. 1. Variation of line spread function with distance from collimator, in air and water. (Source 3 mm in diam., Tc-99m.) At right are also line spread functions as arithmetic means of conjugate depth data for a 20-cm water-filled object. Note that these conjugate functions are approximately uniform, with full width at half maximum of 1.4 cm.

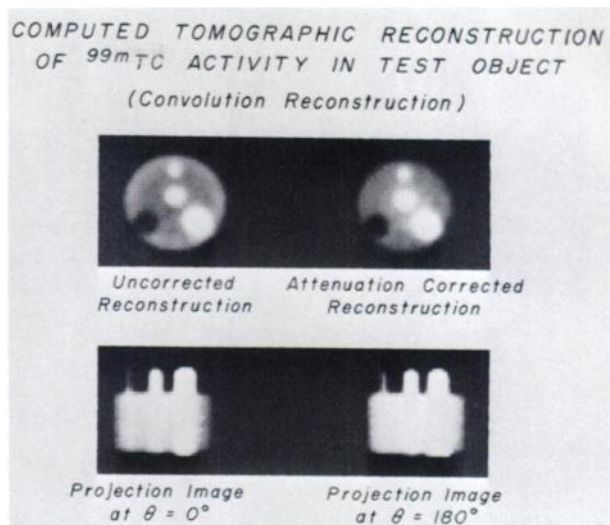


FIG. 2. Top: reconstructions of test object 20 cm in diameter filled with water containing 1 $\mu\text{Ci/cc}$ Tc-99m background activity, three cylinders with diameters 0.95, 1.90, and 3.20 cm filled with 10 $\mu\text{Ci/cc}$ of Tc-99m (hot spots), and one 3.20-cm cylinder containing only water (cold spot). Reconstructions are without and with attenuation correction, performed in a 63 by 63 grid with 7 mm by 7 mm pixel size. Bottom: projection images of these objects at 0° and 180°. Effect of attenuation is evidenced by diminished brightness of largest cylindrical hot spot in 180° view.

arithmetic mean of counts recorded along conjugate views—i.e., summing data recorded 180° apart—to minimize the variations in the line spread function. As indicated in Fig. 1, a uniform line spread function of 1.4 cm (nonuniformities less than 10%) is obtained for the arithmetic mean of conjugate views using a line source in 20 cm of water. A uniform line spread function can also be obtained by forming the geometric mean of conjugate views, and several investigators have reported such results (5,16–18).

The solid angle for collecting the emitted radiation is proportional, approximately, to the inverse square of the distance from the emitting source to the crystal ($1/r^2$), whereas the area a given collimator element can “see” on a distant sheet source varies as the square of the distance (r^2). Therefore, if we define the sensitivity as the product of the solid angle and the amount of activity viewed, the two terms compensate each other as long as there is no attenuation and there is uniform activity within each volume element defined along the field of view. The variation of sensitivity with distance in air is therefore negligible in this context. This argument is supported by an inspection of the area under the line spread functions recorded in air (Fig. 1), which is observed to remain constant (within 5%) with depth.

Evaluation of attenuation-corrected reconstruction technique with test objects (see appendix). Conjugate

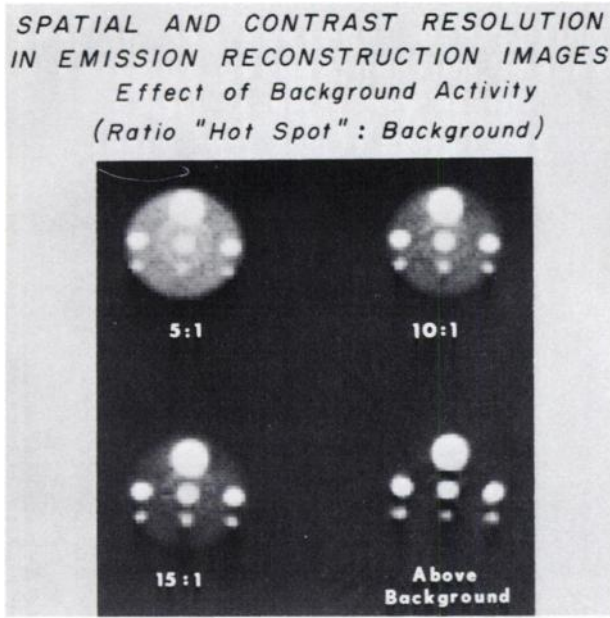


FIG. 3. Attenuation-corrected reconstructions of 20-cm-diameter test object containing rows of cylinders 0.95 and 1.90 cm in diameter, and one 4.30-cm cylinder. All contained water with 10 $\mu\text{Ci/cc}$ of Tc-99m; surrounding background water contained 2, 1, and 0.67 $\mu\text{Ci/cc}$ as the ratios indicate. At bottom right is section lying above background tank. Reconstructions are on 63 by 63 grid with 7 mm by 7 mm pixel size.

views were obtained by rotating the object in front of the gamma camera in 6° steps around 360° and were used to perform reconstructions on a 63 by 63 grid. About 10^6 – 10^7 total counts were used to form each of the transaxial images for test objects. Figure 2 shows reconstructions without and with attenuation correction for a 20-cm-diameter cylinder filled

with water. It contained 1 $\mu\text{Ci/cc}$ of Tc-99m as background activity; hot spots were provided by cylinders 0.95, 1.9, and 3.2 cm in diameter containing 10 $\mu\text{Ci/cc}$, and a cold spot by a 3.2-cm cylinder containing only water. Reconstructions were also performed for a different 20-cm test object that consisted of rows of cylinders 0.95 and 1.9 cm in diameter and another cylinder 4.3 cm in diameter. All the cylinders were filled with water containing 10 $\mu\text{Ci/cc}$ of Tc-99m, while activity was used in the background to provide uptake to background ratios of 5:1, 10:1, and 15:1. The images obtained are shown in Figure 3. Attenuation correction has been performed in these objects using a constant value for μ (0.15 cm^{-1} at 140 keV). Shown in Fig. 4 are reconstructions, without and with attenuation correction, of a 20-cm plexiglass cylinder ($\mu = 0.18 \text{ cm}^{-1}$) in which holes 2 mm in diameter have been drilled and are spaced 2, 3, 4, and 5 cm apart across four diameters. The following conclusions can be drawn from these test-objects studies.

1. The system's response function—measured in terms of the line spread function in the reconstructed images—is uniform (nonuniformities $\sim 10\%$) throughout the cross section and has a full width at half maximum (FWHM) of $\sim 1.8 \text{ cm}$ (Fig. 4).
2. The reconstructed activity values are independent of position within an rms error of 10%. That the variation of sensitivity with depth is negligible (where sensitivity is defined in geometric terms alone, excluding attenuation) is demonstrated by the lower right image of Fig. 3, which represents the reconstruction of a level at which background is absent. No attenuation correction was required

SPATIAL AND CONTRAST RESOLUTION IN EMISSION RECONSTRUCTION IMAGES
Optimization by Use of Conjugate Views and Attenuation Correction

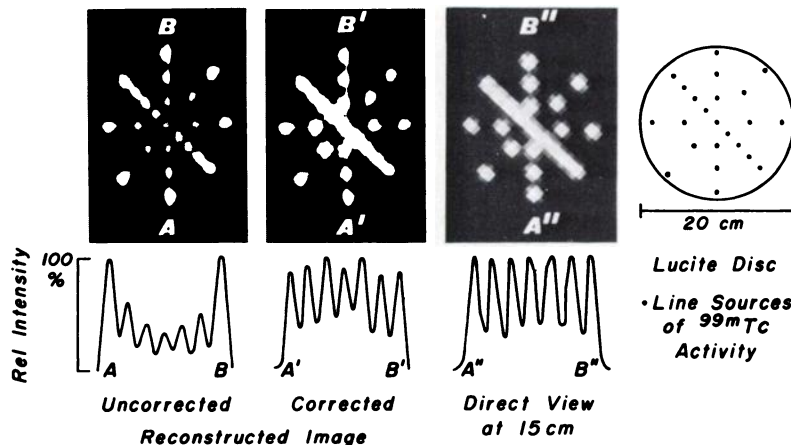


FIG. 4. Attenuation-corrected and uncorrected reconstructions obtained from 20-cm diameter plexiglass "star" phantom with 2-mm holes drilled across four diameters and spaced 2, 3, 4, and 5 cm apart. Holes were filled with equal amounts of Tc-99m. Top row shows uncorrected reconstruction, attenuation-corrected reconstruction, top-view image, and plan drawing of phantom. Below are activity profiles along axis with 3-cm separations, showing uniformity of resolution and intensity obtained throughout reconstructed cross section. "Dip" due to attenuation is seen in uncorrected image, and in profile at left.

since, at this level, the cylinders containing activity protruded above the background water. The reconstructed activity within cylinders of equal size is independent of their location. As demonstrated in all other reconstructed images shown in Figs. 3 and 4, reconstructed activity is independent of depth in the attenuating medium when the attenuation-correction technique is applied.

3. The size of a reconstructed element of activity depends on the true size and the system's response function, which is 1.8 cm in the reconstructed images for the present imaging system. To a first approximation, the reconstructed FWHM of an object containing activity is the result of a quadrature summation of the FWHM of the system's response function and the actual size of the object. From Figs. 2 and 3, cylinders of diameters 4.5, 3.2, 1.9, and 0.95 cm were reconstructed giving FWHM sizes of 4.62, 3.5, 2.6, and 2.1 cm, respectively. Quadrature subtraction of the system's response function yielded 4.25, 3.00, 1.88, and 1.08 cm, respectively, for the estimated true sizes. The average rms error in this computation was about 10%, with the smallest objects' size being reconstructed with greater uncertainty.

4. The computed values of the uptake exhibit a size-dependent effect, as is apparent from Figs. 2 and 3. For objects of diameter 4.3 cm or larger (i.e., roughly 2.5 times the system's response function), the reconstructed activity concentration varies linearly as a function of the true value. For objects smaller than 4.3 cm, the reconstructed activity values were found to vary in a nonlinear but monotonic and reproducible manner with the true activity. Since the true size of an activity distribution can be determined accurately, the absolute value of the activity concentration can be obtained, if desired, from a "look-up" table that relates size to true uptake (19).

Myocardial infarct studies in dogs. Conventionally two-dimensional PPI scintigrams with at most four angles of view, are used for acute myocardial infarction studies. It is very difficult, however, to obtain quantitative estimates of the location and extent of infarction from projection images, since superimposed activity from the bones is difficult to subtract accurately and the infarcted region can have a high degree of asymmetry in any direction. We have used computerized transaxial reconstruction techniques to obtain quantitative estimates of surgically-induced acute myocardial infarcts in dogs. The proximal left anterior descending coronary artery was ligated in five dogs, the left circumflex artery in one dog, and a sham operation was used in a seventh dog as a control. About 24 hr postligation the dogs were injected intravenously

with approximately 30 mCi of PPI. Two hours were allowed for the blood pool to clear; then the dogs were killed and rotated in an erect position in front of a prototype cylindrical x-ray computed tomographic scanner (14). From this, multiple parallel transaxial levels of x-ray attenuation coefficients over the entire thorax of each dog were reconstructed for 120-kVp x-rays (mean energy \approx 73 keV (20)). Maps of attenuation coefficients at 140 keV were obtained by linear extrapolation of these values. With this procedure the attenuation coefficients for most biologic tissues can be obtained to an rms error of 10-15%, and the resulting data were used to correct the emission images for attenuation. Reported values of attenuation coefficients for biologic substances over the range 18-136 keV (21) support the basic assumption. The dogs were then scanned in the same upright position, using the gamma camera, in steps of 6° around 360°. Vertical levels of the emission and transmission images were aligned by using radioactive markers and lead beads, respectively, and the resulting images were subsequently registered to achieve superposition. Data were collected for about 100-150 sec at each angle of view. Since 6-8 hr elapsed between administration of the activity and commencement of scanning, the counting rate obtained was equivalent to that obtainable if 15 mCi of activity had been administered.

A set of emission and transmission images at

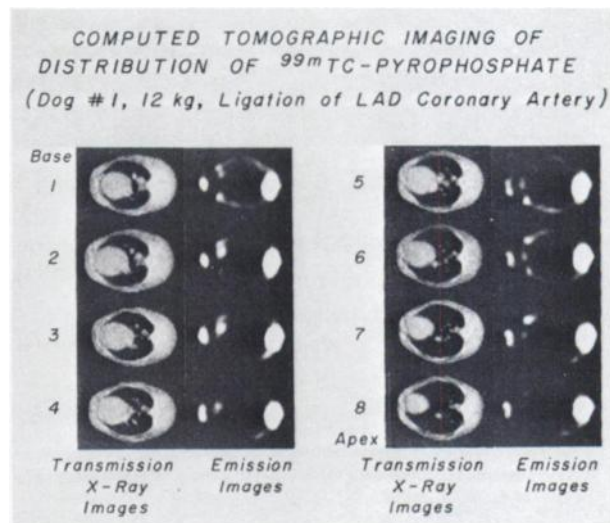


FIG. 5. Eight corresponding emission and transmission reconstructed levels through thorax of dog with infarct (ligation of the left anterior descending artery). X-ray transmission images at the left show structure; emission transaxial images at right are corrected for attenuation using values from transmission image. Sections 14 mm thick, spacing 7 mm (overlapping), extending from base to apex of heart. Note location and extent of Tc-99m PPI uptake into the infarct, as well as into ribs, sternum, and spine.

multiple corresponding levels is shown in Fig. 5 for a dog with a large infarct. Approximately 25 overlapping slices of 1.4 cm thickness, spaced 0.7 cm apart and thus covering about 17 cm axial extent of the thorax, were computed for emitted photons, and 25 corresponding 0.7-cm slices were computed for transmitted x-rays. The eight levels containing the heart are shown in Fig. 5. For dogs used in this study, counts in profile data at any angle of view occupied less than 32 of the 64 pixels across which digitization was performed. A linear interpolation of the profile data was performed to increase the sampling frequency by a factor of two, and reconstructions were obtained on a 63 by 63 grid with a pixel size of 3.5×3.5 mm. Compared with images obtained on 7- by 7-mm pixels without interpolation, this procedure produced images with a smoother texture, afforded greater accuracy for matching the emission and transmission images and carrying out the attenuation correction procedure, and did not degrade resolution or increase noise. The total counts per level in the emission images was about 3 million, and typically the boundary of the dog contained 2000 pixels. Thus the rms uncertainty is expected to be about 19% (22). However, as pointed out by Budinger (23), the activity is not distributed uniformly but is concentrated in small portions of the image. The rms uncertainty, therefore, may be lower by about a factor of three in a practical imaging situation.

Uptake in the infarcted region, sternum, ribs, and the backbone is clearly visualized in the emission images, while the transmission images show the epicardial surface, the pleural surface of the lungs, the esophagus, and the airway. No uptake in the myocardium was seen in the control dog. A rather dramatic demonstration of the potential of transaxial images is shown by the images of a dog with a small (approximately 2-3 g) inferior infarct produced by ligation of the left circumflex coronary artery. This infarct could not be distinguished from the surrounding structures in any of the projection images, examples of which are shown in Fig. 6, whereas it is clearly shown in the reconstructed images. The infarcted regions were outlined by thresholding at 50% level (FWHM) to determine edges. To a first approximation, the outline defined an ellipse at each transaxial level. Quantitative estimates of the size were then obtained by a quadrature subtraction of the system's response function, as discussed in the section dealing with test-object studies.

Histopathologic procedures. Pathologic and histologic estimates of the infarcted region were obtained in the following way.

The ventricles were cut into five or more trans-

verse slices, perpendicular to the long axis of the heart, so that each segment contained portions of the right and left ventricular free walls and the interventricular septum. Each slice was approximately 1-1.5 cm in thickness. They were stained for dehydrogenase activity (24), divided into 16 sub-units (segments) (25,26), and the relative proportion of grossly visible intrasegmental damage estimated by visual inspection as judged by the absence of tetrazolium staining and the presence of gross discoloration of the cut myocardial surface.

Paraffin sections were prepared from the middle third of all slices demonstrating grossly injured myocardium, or containing significant radioactivity, or forming a boundary of such segments. These were stained by the hematoxylin and eosin and the PAS methods, and the proportion of myocardial injury was estimated by light microscopy.

The weight of myocardial injury within each segment was computed as the estimated percentage of injury of the segment (gross or microscopic) multiplied by segment weight. The total weight of myocardial injury was computed as the sum of the segmental estimates. In Fig. 7 the estimated mass of the infarcted region (as determined from the volume of the region outlined by PPI activity in the reconstructed images) is plotted against the microscopic estimations of myocardial injury. A linear regression analysis shows a high correlation ($r^2 = 0.99$) between the two quantities.

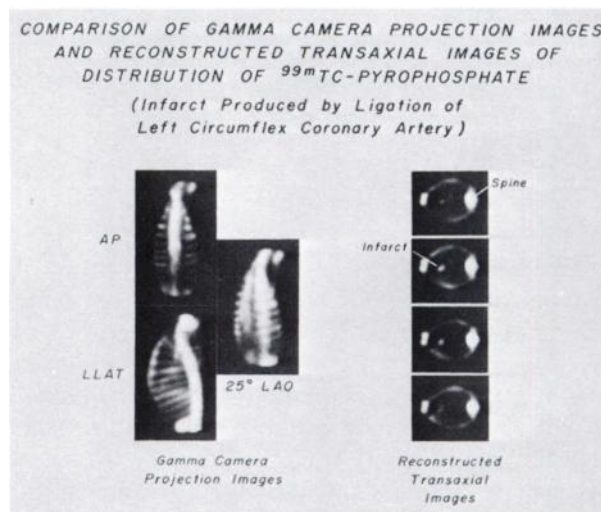


FIG. 6. Comparison between conventional scintiphotos and reconstructed images of Tc-99m PPI in thorax of dog with small myocardial infarct (ligation of the left circumflex coronary artery). Emission computed tomography provides potential increase in diagnostic sensitivity: gamma-camera images at left do not show this small inferior infarct, but reconstructed images calculated from 60 such projections clearly show uptake of PPI in infarct in the four levels shown at right. Subsequent examination by PAS staining techniques confirmed presence of small (~2-g) infarct.

COMPARISON OF ESTIMATES OF MASS OF INJURED MYOCARDIUM USING ^{99m}Tc-PYROPHOSPHATE EMISSION COMPUTED TOMOGRAPHY AND HISTOLOGICAL STAINING TECHNIQUES (7 Dogs, 12-15 kg)

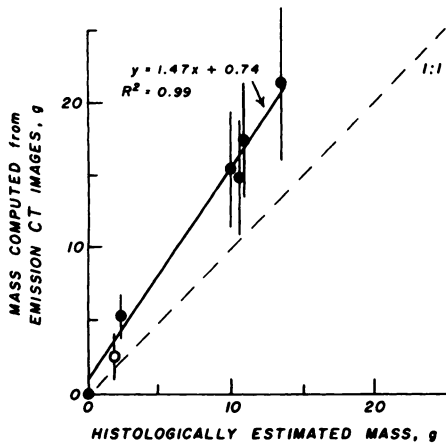


FIG. 7. Plot of estimated sizes of infarcted region, as determined from the uptake of Tc-99m PPI in reconstructed images, against histological estimates by PAS staining techniques. Radionuclide estimates are consistently greater. Linear regression analysis shows high correlation ($r^2 = 0.99$) between the two determinations. Data point for animal infarcted by ligation of left circumflex coronary is shown as open circle.

Poliner et al. (27) obtained a significant correlation between the histologically-determined infarct weight and area of PPI uptake as determined from the scintigraphic projection view with the largest measured infarct area. Their technique, however, ignores the three-dimensional nature of infarction and is therefore expected to be relatively inaccurate—particularly for nontransmural or subendocardial infarcts. In an attempt to overcome this problem, Lewis et al. (28) developed a simple technique for three-dimensional sizing using two orthogonal views and obtained good correlation between a histologic estimate of infarct mass and infarct volume predicted from their model. No attempt was made to compute the infarct mass directly from the predicted volume. A simple conversion of their data from volume to mass as predicted by the PPI scan indicates a significant overestimation of infarct mass. Siemers et al. (29) report a poor correlation for the linear relationship between the volume delineated by the PPI activity (as determined by imaging cross-sectional slices of excised dog hearts) and the volume calculated by histochemical study. The volume by radionuclide scan was, on the average, 2.8 times that obtained histologically in their measurement.

Our results indicate a good correlation between the radionuclide-estimated volume and the histolog-

ically-estimated volume of the injury. They also indicate that the radionuclide estimated sizes are consistently greater than the histologically estimated sizes.

APPENDIX

Attenuation-correction technique. Photons originating from each volume element of the body are attenuated by tissues interposed between the origin and the boundary. It is necessary, therefore, to make corrections for this effect in order to obtain quantitative results. Budinger and Gullberg (3) have outlined eight methods for attenuation correction. We have developed a different technique for use with a convolution reconstruction algorithm in which the contribution received by each pixel is appropriately weighted in the back-projection step to compensate for attenuation. Mathematically the procedure can be explained in the following way.

Let

- A_i = activity contained in the i th volume element of the object;
- $p^{k,\theta}$ = profile data—i.e., sum of activity measured along the k th ray at angle of view θ ;
- $f_i^{k,\theta}$ = fractional volume of the i th element that is contained within the k th ray;
- μ_i = the attenuation coefficient for the i th element corresponding to the energy of the emitted photon;
- $l_i^{k,\theta}$ = length of that portion of the k th ray that is contained within the i th element; the attenuation suffered by the k th ray while traversing the i th element is therefore $e^{-\mu_i l_i^{k,\theta}}$;
- $\exp - [\sum_j \mu_j l_j^{k,\theta}]$ = attenuation factor for radiation originating from the i th element; the index j denotes elements lying along the k th ray between the i th element and the boundary of the object nearest the detector.

Therefore,

$$p^{k,\theta} = \sum_{i \in k,\theta} f_i^{k,\theta} A_i \exp - [\sum_j \mu_j l_j^{k,\theta}], \quad (1)$$

where ϵ means "is an element of the set of points."

Similarly, for the conjugate view we have

$$P_c^{k,\theta} = \sum_{i \in k,\theta} f_i^{k,\theta} A_i [\exp - (\sum_j \mu_j l_j^{k,\theta})]_c, \quad (2)$$

where the subscript c denotes conjugate views.

The arithmetic mean of the counts recorded along channel k at each angle of view θ is therefore given by the following expression:

$$2 \bar{P}^{k,\theta} = p^{k,\theta} + P_c^{k,\theta} = \sum_{i \in k,\theta} f_i^{k,\theta} A_i \{ [\exp - (\sum_j \mu_j l_j^{k,\theta})] + [\exp - (\sum_j \mu_j l_j^{k,\theta})]_c \}, \quad (3)$$

where the factor of 2 can be dropped, since it appears in all the profiles.

Normally all $P^{k,\theta}$ are convolved with a filter function and back-projected to obtain a transaxial image. In our scheme, the profile data are also convolved in a normal way using the Ramchandran-Lakshminarayanan kernel (30). However, in the backprojection step the contribution received by each pixel is weighted by a factor that is the reciprocal of the attenuation factor in Eq. 3—i.e., by

$$\{ [\exp - (\sum_j \mu_j l_j^{k,\theta})] + [\exp - (\sum_j \mu_j l_j^{k,\theta})]_c \}^{-1}.$$

This procedure is carried out for every pixel in each projection. The map of attenuation coefficients required for this procedure was either known (in the case of test objects with known composition) or obtained from a separate x-ray transmission CT scan.

ACKNOWLEDGMENTS

The authors express their appreciation to Miss Patricia Snider and Mrs. Donna Balow and their coworkers for their help with secretarial work and illustrations, and to Messrs. Julijis Zarins, Donald Hegland, and Don Erdman for their efforts regarding experimental preparations and in the collection of the experimental data.

This research was supported in part by Grants NIH HL-04664, HL-07111 and RR-00007 from the National Institutes of Health. Dr. Singh was the recipient of an American Heart Association Visiting Scientist Award, Dr. Gustafson was the recipient of an American Heart Association Career Investigator Fellowship, both sponsored by Dr. Earl H. Wood, a career investigator of the American Heart Association, Award AHA CI-10.

REFERENCES

1. KUHL DE, EDWARDS RQ: Image separation radioisotope scanning. *Radiology* 80: 653-662, 1963
2. CHESLER DA: Positron tomography and three-dimensional reconstruction technique. In *Tomographic Imaging in Nuclear Medicine*, Freedman GS, ed. New York, Society of Nuclear Medicine, 1973, pp 176-183
3. BUDINGER TF, GULLBERG GT: Three-dimensional reconstruction in nuclear medicine emission imaging. *IEEE Transactions in Nuclear Science* NS-21(3): 2-20, 1974
4. BUDINGER TF, HARPOOTLIAN J: Transverse section reconstruction from multiple gamma-camera views using frequency filtering. *Lawrence Berkeley Laboratory Report No. LBL-2862*, 1975
5. JASZCZAK RJ, MURPHY PH, HUARD D, et al: Radionuclide emission computed tomography of the head with ^{99m}Tc and a scintillation camera. *J Nucl Med* 18: 373-380, 1977
6. KEYES JW JR, ORLANDEA N, HEETDERKS WJ, et al: The humongotron. A scintillation-camera transaxial tomograph. *J Nucl Med* 18: 381-387, 1977
7. KUHL DE, EDWARDS RQ, RICCI AR, et al: The Mark IV system for radionuclide computed tomography of the brain. *Radiology* 121: 405-413, 1976
8. BROWNELL GL, BURNHAM CA, WILENSKY S, et al: New developments in positron scintigraphy and the application of cyclotron produced positron emitters. *Medical Radioisotope Scintigraphy*, Vienna, IAEA, 1: 163-176, 1969
9. TER-POGOSSIAN MM, PHELPS ME, HOFFMAN EJ, et al: A positron-emission transaxial tomography for nuclear imaging (PETT). *Radiology* 114: 89-98, 1975
10. CHO ZH, COHEN MB, SINGH M, et al: Performance and evaluation of the circular ring transverse axial positron camera (CRTAPC). *IEEE Transactions in Nuclear Science* NS-24(1): 532-543, 1977
11. DERENZO SE, BUDINGER TF, CAHOON JL, et al: High resolution computed tomography of positron emitters. *IEEE Transactions in Nuclear Science* NS-24(1): 544-558, 1977
12. TER-POGOSSIAN MM: Limitations of present radionuclide methods in the evaluation of myocardial ischemia and infarction. *Circulation* 53(Suppl No 1): 119-121, 1976
13. PHELPS ME, HOFFMAN EJ, MULLANI NA, et al: Application of annihilation coincidence detection to transaxial reconstruction tomography. *J Nucl Med* 16: 210-224, 1975
14. STURM RE, RITMAN EL, JOHNSON SA, et al: Prototype of a single x-ray video imaging chain designed for high temporal resolution computerized tomography by means of an electronic scanning dynamic spatial reconstruction system. *Proceedings of the San Diego Biomedical Symposium* (February 4-6, 1976, San Diego, California) 15: 181-188
15. KAY DB, KEYES JW, JR: First order corrections for absorption and resolution compensation in radionuclide Fourier tomography. *J Nucl Med* 16: 540-541, 1975 (Abst)
16. KEYES WI: A practical approach to transverse-section gamma-ray imaging. *Brit J Radiol* 49: 62-70, 1976
17. BUDINGER TF, DERENZO SE, GULLBERG GT, et al: Emission computed axial tomography. *IAEA Symposium on Medical Radionuclide Imaging*, October 25-29, 1976, Los Angeles, IAEA-SM-210/124 Medical Radionuclide Imaging, Vienna IAEA 1: 321, 1977 (Abst)
18. KAY DB, THOMPSON BJ: Optical processing in radionuclide tomographic image reconstruction. *Optical Engineering* 16(1): 45-51, 1977
19. GUSTAFSON DE, BERGGREN MJ, SINGH M, et al: Computerized transaxial imaging using single gamma emitters (Presented at 63rd Scientific Assembly and Annual Meeting of the RSNA). *Radiology* 129: 187-194, 1978
20. McCULLOUGH EC, PAYNE JT, BAKER HL, JR, et al: Performance evaluation and quality assurance of computed tomography scanners, with illustrations from the EMI, ACTA, and Delta scanners. *Radiology* 120: 173-188, 1976
21. PHELPS ME, HOFFMAN EJ, TER-POGOSSIAN MM: Attenuation coefficients of various body tissues, fluids, and lesions at photon energies of 18 to 136 keV. *Radiology* 117: 573-583, 1975
22. HUESMAN RH: The effects of a finite number of projection angles and finite lateral sampling of projections on the propagation of statistical errors in transverse section reconstruction. *Phys Med Biol* 22: 511-521, 1977
23. BUDINGER TF: Current and future application of reconstruction techniques. *Proc FASEB Symposium* (Anaheim, California, 1976): in press
24. LIE JT, PAIROLERO PC, HOLLEY KE, et al: Macroscopic enzyme-mapping verification of large, homogeneous experimental myocardial infarcts of predictable size and location in dogs. *J Thorac Cardiovasc Surg* 69: 599-605, 1975
25. BIZARRO RO: Myocardial scar, morphologic and vectorcardiographic study. M.S. Thesis. University of Minnesota Graduate School, 1971
26. DESILVA NA: A quantitative morphologic, vectorcardiographic and clinical study of some malconformations of the human myocardium. M.S. Thesis. University of Minnesota Graduate School, 1974
27. POLINER LD, BUJA LM, PARKEY RW, et al: Comparison of different noninvasive methods in infarct sizing during experimental myocardial infarction. *J Nucl Med* 18: 517-523, 1977
28. LEWIS M, BUJA LM, SAFFER S, et al: Experimental infarct sizing using computer processing and a three-dimensional model. *Science* 197: 167-169, 1977
29. SIEMERS PT, HIGGINS CB, SCHMIDT W, et al: Detection, quantitation and contrast enhancement of myocardial infarction utilizing computerized axial tomography: comparison with histochemical staining and ^{99m}Tc -Pyrophosphate imaging. *Invest Radiol* 13(2): 103-109, 1978
30. RAMCHANDRAN GN, LAKSHMINARAYANAN AV: Three-dimensional reconstruction for radiographs and electron micrographs: Application of convolutions instead of Fourier transforms. *Proc Natl Acad Sci USA* 68: 2236-2240, 1971